

Kinetic temperature of massive star forming molecular clumps measured with formaldehyde

X. D. Tang^{1,2,3}, C. Henkel^{1,4}, K. M. Menten¹, X. W. Zheng⁵, J. Esimbek^{2,3}, J. J. Zhou^{2,3}, C. C. Yeh¹, C. König¹, Y. Yuan^{2,3}, Y. X. He^{2,3}, and D. L. Li^{2,3}

¹ Max-Planck-Institut für Radioastronomie, Auf dem Hügel 69, 53121 Bonn, Germany
e-mail: xdtang@mpi-fr-bonn.mpg.de

² Xinjiang Astronomical Observatory, Chinese Academy of Sciences, 830011 Urumqi, China

³ Key Laboratory of Radio Astronomy, Chinese Academy of Sciences, 830011 Urumqi, China

⁴ Astronomy Department, King Abdulaziz University, PO Box 80203, 21589 Jeddah, Saudi Arabia

⁵ Department of Astronomy, Nanjing University, 210093 Nanjing, China

March 6, 2024

ABSTRACT

Context. For a general understanding of the physics involved in the star formation process, measurements of physical parameters such as temperature and density are indispensable. The chemical and physical properties of dense clumps of molecular clouds are strongly affected by the kinetic temperature. Therefore, this parameter is essential for a better understanding of the interstellar medium. Formaldehyde, a molecule which traces the entire dense molecular gas, appears to be the most reliable tracer to directly measure the gas kinetic temperature.

Aims. We aim to determine the kinetic temperature with spectral lines from formaldehyde and to compare the results with those obtained from ammonia lines for a large number of massive clumps.

Methods. Three 218 GHz transitions ($J_{K_A K_C} = 3_{03}-2_{02}$, $3_{22}-2_{21}$, and $3_{21}-2_{20}$) of para-H₂CO were observed with the 15m James Clerk Maxwell Telescope (JCMT) toward 30 massive clumps of the Galactic disk at various stages of high-mass star formation. Using the RADEX non-LTE model, we derive the gas kinetic temperature modeling the measured para-H₂CO $3_{22}-2_{21}/3_{03}-2_{02}$ and $3_{21}-2_{20}/3_{03}-2_{02}$ ratios.

Results. The gas kinetic temperatures derived from the para-H₂CO ($3_{21}-2_{20}/3_{03}-2_{02}$) line ratios range from 30 to 61 K with an average of 46 ± 9 K. A comparison of kinetic temperature derived from para-H₂CO, NH₃, and the dust emission indicates that in many cases para-H₂CO traces a similar kinetic temperature to the NH₃ (2,2)/(1,1) transitions and the dust associated with the HII regions. Distinctly higher temperatures are probed by para-H₂CO in the clumps associated with outflows/shocks. Kinetic temperatures obtained from para-H₂CO trace turbulence to a higher degree than NH₃ (2,2)/(1,1) in the massive clumps. The non-thermal velocity dispersions of para-H₂CO lines are positively correlated with the gas kinetic temperature. The massive clumps are significantly influenced by supersonic non-thermal motions.

Key words. Stars: formation – Stars: massive – ISM: clouds – ISM: molecules – ISM: abundances – radio lines: ISM

1. Introduction

Ammonia (NH₃) is frequently used as the standard molecular cloud thermometer (Ho & Townes 1983; Walmsley & Ungerechts 1983; Danby et al. 1988; Mangum et al. 2013b). However, its abundance can vary strongly in different environments (e.g., 10^{-5} in hot cores; Mauersberger et al. 1987 and 10^{-8} in dark clouds; Benson & Myers 1983) and is extremely affected by a high UV flux. Species like CH₃C₂H and CH₃CN, also sensitive to kinetic temperature, are not widespread enough (e.g., Güsten et al. 1985; Bally et al. 1987; Nummelin et al. 1998). Therefore, these molecules are of limited use as reliable probes to trace the gas kinetic temperature (Mangum et al. 1993).

Formaldehyde (H₂CO) is a ubiquitous molecule in molecular clouds (Downes et al. 1980; Cohen & Few 1981; Bieging et al. 1982; Cohen et al. 1983; Zylka et al. 1992; Mangum et al.

2008; Ao et al. 2013; Mangum et al. 2013a; Tang et al. 2013; Ginsburg et al. 2015, 2016). It is thought to be formed on the surface of dust grains by successive hydrogenation of CO (Watanabe & Kouchi 2002; Woon 2002; Hidaka et al. 2004), it is released into the gas phase by shocks or UV heating, and is destroyed by photodissociation. Unlike for NH₃, the fractional abundance of H₂CO does not vary substantially and is similar even when comparing e.g., the hot core with the compact ridge of the well-studied Orion-KL nebula (Mangum et al. 1990; Mangum & Wootten 1993; Caselli et al. 1993; Johnstone et al. 2003).

Since the relative populations of the K_a ladders of H₂CO are governed by collisions, line ratios involving different K_a ladders are good tracers of the kinetic temperature (Mangum et al. 1993; Mühle et al. 2007). Particularly useful are the three transitions of para-H₂CO ($J_{K_A K_C} = 3_{03}-2_{02}$, $3_{22}-2_{21}$, and $3_{21}-2_{20}$), which can be measured simultaneously at ~ 218 GHz with a

Table 1. Source parameters.

Sources	RA(J2000) h m s	DEC(J2000) ° ′ ″	$N(\text{NH}_3)$ 10^{15} cm^{-2}	$N(\text{H}_2)$ 10^{22} cm^{-2}	$S_{870\mu\text{m}}$ Jy	$T_{\text{kin}}(\text{NH}_3)$ K	$T_{\text{dust}}(\text{HiGal})$ K	Distance kpc	Association
G5.89-0.39	18:00:30.34	-24:04:00.21	2.29	87.19	41.64	39.7±3.2	54.1±4.1	2.47	HII
G5.90-0.44	18:00:43.60	-24:04:51.09	1.95	34.36	14.74	31.5±2.6	33.3±6.5	2.45	HII
G5.97-1.36	18:04:22.14	-24:28:28.28	3.16	5.80	2.72	37.9±26.3	30.0	13.8	
G6.91-0.22	18:02:05.32	-23:05:18.03	3.98	18.53	4.65	15.6±0.8	12.2±0.8	3.86	
G9.04-0.52	18:07:42.14	-21:23:00.84	3.16	11.74	2.70	14.4±0.7	19.6±4.5	12.21	IRDC
G9.21-0.20	18:06:52.03	-21:04:27.35	3.72	18.04	5.37	18.6±1.0	27.0±2.4	11.95	IRDC
G9.88-0.75	18:10:18.87	-20:45:24.26	2.88	23.84	8.44	23.1±1.4	26.1±3.9	3.72	IRDC
G10.99-0.08	18:10:06.50	-19:27:46.24	4.68	14.74	2.87	12.6±0.5	11.4±0.6	3.67	IRDC
G11.92-0.61	18:13:58.04	-18:54:24.91	2.82	32.66	10.93	21.4±1.1	23.3±0.1	3.91	EGO
G12.43-1.11	18:16:51.70	-18:41:26.52	1.05	19.30	7.91	29.0±3.0	...	12.5	HII
G12.68-0.18	18:13:53.79	-18:01:52.60	6.92	26.61	11.51	32.1±6.4	27.7±3.9	4.85	IRDC
G12.91-0.26	18:14:39.34	-17:52:04.53	3.55	50.29	20.17	28.0±1.7	28.1±4.2	3.85	EGO
G13.28-0.30	18:15:39.85	-17:34:34.89	2.95	10.76	2.29	13.5±0.6	11.1±0.3	4.04	IRDC
G14.20-0.19	18:16:58.91	-16:42:08.26	3.39	22.53	7.30	20.6±0.8	23.1±0.5	3.83	IRDC, EGO?
G14.33-0.64	18:18:54.52	-16:47:41.24	2.57	67.36	25.52	25.5±1.4	27.3±7.5	2.55	EGO
G15.66-0.50	18:20:59.44	-15:33:14.52	2.82	14.34	5.30	24.6±1.0	26.3	0.08	IRDC
G17.10+1.02	18:18:14.80	-13:34:14.51	3.16	2.05	1.13	60.6±62.1	28.1±1.1	2.05	
G18.21-0.34	18:25:21.56	-13:13:39.55	2.29	14.00	3.90	17.3±1.5	10.5±0.2	12.34	IRDC
G19.01-0.03	18:25:44.48	-12:22:42.20	2.14	17.24	5.35	19.5±1.1	26.4±4.3	4.37	HII, EGO?
G22.55-0.52	18:34:12.70	-09:28:21.49	2.69	11.58	3.09	16.6±0.7	24.7±1	10.84	IRDC
G28.61-0.03	18:43:37.56	-03:51:37.98	2.19	...	1.05	41.2±16.0	29.3±5	11.81	
G28.86+0.07	18:43:46.02	-03:35:29.79	3.63	...	7.56	48.4±6.8	33.2±4.3	6.28	HII
G30.24+0.57	18:44:29.16	-02:08:22.85	3.02	2.23	1.04	37.6±14.6	28.1±4.2	13.36	
G30.70-0.07	18:47:36.16	-02:00:58.22	8.13	73.44	28.37	26.3±2.2	40.0	5.64	IRDC
G31.40-0.26	18:49:33.05	-01:29:03.02	2.40	21.14	9.58	35.2±2.9	29.8±3.4	5.41	HII
G31.70-0.49	18:50:56.88	-01:19:17.41	1.62	6.60	1.16	11.7±0.8	13.7±4.3	4.99	IRDC
G34.37-0.66	18:56:25.80	+00:58:41.43	9.33	7.47	1.12	10.5±0.9	33.0±6.5	0.84	IRDC
G35.03+0.35	18:54:00.63	+02:01:21.85	1.86	19.49	8.62	33.5±4.5	39.2	3.49	EGO
G35.19-0.74	18:58:11.96	+01:40:23.87	2.04	27.21	10.73	27.2±1.5	32.1±10.3	2.31	HII, EGO
G37.87-0.40	19:01:53.62	+04:12:51.45	1.00	...	10.08	33.9±8.2	36.7±4.6	9.38	HII

Notes. Parameters related to NH_3 , $N(\text{H}_2)$, and $S_{870\mu\text{m}}$ are selected from Wienen et al. (2012). Distances are the kinematic distances presented by Wienen et al. (2015). Last column: HII = HII region, IRDC = infrared dark cloud, EGO = extended green object.

bandwidth of 1 GHz and whose relative strengths ($\text{para-H}_2\text{CO}$ $3_{22-2_{01}}/3_{03-2_{02}}$ and $3_{21-2_{00}}/3_{03-2_{02}}$) provide a sensitive thermometer, possibly the best of the very few that are available for the analysis of dense molecular gas. In the case of optically thin emission, the line ratios are sensitive to gas kinetic temperatures $\lesssim 50$ K with a small measurement uncertainty (Mangum et al. 1993), which is similar to the kinetic temperature range that the NH_3 (2,2)/(1,1) ratio is sensitive to (Ho & Townes 1983; Mangum et al. 1992, 2013a).

Measurements of the dense molecular ridge in NGC2024 with the $\text{para-H}_2\text{CO}$ ($3_{03-2_{02}}$ and $3_{22-2_{01}}$) transitions show that the derived kinetic temperatures are warmer ($T_{\text{kin}}(\text{H}_2\text{CO}) \sim 45 - 85$ K; Watanabe & Mitchell 2008) than those traced by NH_3 (2,2)/(1,1) ($T_{\text{kin}}(\text{NH}_3) \sim 27 - 55$ K; Schulz et al. 1991). Using the three transitions of $\text{para-H}_2\text{CO}$ at ~ 218 GHz to measure the kinetic temperature of the starburst galaxy M82 shows that the derived kinetic temperature ($T_{\text{kin}}(\text{H}_2\text{CO}) \sim 200$ K; Mühle et al. 2007) is significantly higher than the temperature deduced from the NH_3 (1,1)-(3,3) lines ($T_{\text{kin}}(\text{NH}_3) \sim 60$ K; Weiß et al. 2001) and the dust temperature ($T_{\text{dust}} \sim 48$ K; Colbert et al. 1999). It is the higher T_{kin} value from H_2CO which is representative for the bulk of the molecular gas in M82 (Mühle et al. 2007). Ao et al. (2013) and Ginsburg et al. (2016) used the same $\text{para-H}_2\text{CO}$ transitions to measure the kinetic temperature of the dense molecular clouds near the Galactic center. They found that these H_2CO -derived gas kinetic temperatures (average ~ 65 K) are uniformly higher than the NH_3 (2,2)/(1,1) temperatures and the dust temperatures of 14 – 30 K. Overall, $\text{para-H}_2\text{CO}$, a molecule

which traces the entire dense molecular gas without much bias because of a lack of drastic changes in abundance, appears to be the best long-sought tracer of kinetic temperature of the dense molecular gas at various stages of star formation.

The APEX Telescope Large Area Survey of the GALaxy (ATLASGAL) (Schuller et al. 2009), using the Large APEX Bolometer Camera (LABOCA) at $870 \mu\text{m}$ (Siringo et al. 2009), presents observations in a Galactic longitude range of $\pm 60^\circ$ and latitude range of $\pm 1.5^\circ$. This introduces a global view of star formation at submm wavelengths and identifies a large number of massive clumps forming high-mass stars at various stages in the inner Galaxy (Contreras et al. 2013; Urquhart et al. 2014; Csengeri et al. 2014). In this paper, we aim to measure the kinetic temperature with three transitions of $\text{para-H}_2\text{CO}$ ($J_{K_A K_C} = 3_{03-2_{02}}$, $3_{22-2_{01}}$, and $3_{21-2_{00}}$) toward the massive clumps selected from the ATLASGAL survey. Our main goals are the following: (a) determining to what degree the kinetic temperatures obtained from NH_3 and from $\text{para-H}_2\text{CO}$ differ from each other, (b) seeking a correlation between the temperature of the gas and that of the dust, and (c) searching for a correlation between kinetic temperature and line width as is expected in the case of conversion of turbulent energy into heat. In Sections 2 and 3, we introduce our observations of the $\text{para-H}_2\text{CO}$ triplet and the data reduction, and describe the main results. The comparison of kinetic temperatures derived from $\text{para-H}_2\text{CO}$, NH_3 , and dust is discussed in Section 4. Our main conclusions are summarized in Section 5.

Table 2. Para-H₂CO spectral parameters.

Sources	Transition	$\int T_{\text{mb}} dv$ K km s ⁻¹	V_{lsr} km s ⁻¹	FWHM km s ⁻¹	T_{mb} K
G5.89-0.39	3 ₀₃ – 2 ₀₂	44.80(2.27)	10.40(0.18)	7.47(0.46)	5.63
	3 ₂₂ – 2 ₂₁	11.01(0.23)	9.40(0.06)	5.54(0.14)	1.87
	3 ₂₁ – 2 ₂₀	11.47(0.23)	9.39(0.05)	5.61(0.14)	1.91
G5.90-0.44	3 ₀₃ – 2 ₀₂	7.96(0.67)	10.39(0.20)	4.78(0.47)	1.57
	3 ₂₂ – 2 ₂₁	0.61(0.13)	9.59(0.18)	1.94(0.50)	0.30
	3 ₂₁ – 2 ₂₀	1.41(0.21)	9.85(0.34)	4.83(0.98)	0.27
G5.97-1.36	3 ₀₃ – 2 ₀₂	3.93(0.11)	14.18(0.03)	2.19(0.08)	1.69
	3 ₂₂ – 2 ₂₁
	3 ₂₁ – 2 ₂₀
G6.91-0.22	3 ₀₃ – 2 ₀₂	2.99(0.20)	21.26(0.16)	5.14(0.39)	0.54
	3 ₂₂ – 2 ₂₁
	3 ₂₁ – 2 ₂₀
G9.04-0.52	3 ₀₃ – 2 ₀₂	0.80(0.13)	37.41(0.17)	2.28(0.56)	0.33
	3 ₂₂ – 2 ₂₁
	3 ₂₁ – 2 ₂₀
G9.21-0.20	3 ₀₃ – 2 ₀₂	1.00(0.14)	42.44(0.17)	2.38(0.37)	0.40
	3 ₂₂ – 2 ₂₁
	3 ₂₁ – 2 ₂₀
G9.88-0.75	3 ₀₃ – 2 ₀₂	6.43(0.27)	28.47(0.07)	3.82(0.22)	1.59
	3 ₂₂ – 2 ₂₁
	3 ₂₁ – 2 ₂₀
G11.92-0.61	3 ₀₃ – 2 ₀₂	3.76(0.20)	35.99(0.09)	3.49(0.23)	1.01
	3 ₂₂ – 2 ₂₁
	3 ₂₁ – 2 ₂₀
G12.43-1.11	3 ₀₃ – 2 ₀₂	7.40(0.17)	40.26(0.03)	3.35(0.10)	2.07
	3 ₂₂ – 2 ₂₁
	3 ₂₁ – 2 ₂₀
G12.68-0.18	3 ₀₃ – 2 ₀₂	4.31(0.21)	54.85(0.13)	5.84(0.41)	0.70
	3 ₂₂ – 2 ₂₁
	3 ₂₁ – 2 ₂₀
G12.91-0.26	3 ₀₃ – 2 ₀₂	12.53(0.40)	37.24(0.08)	5.02(0.21)	2.34
	3 ₂₂ – 2 ₂₁	2.17(0.19)	37.76(0.13)	3.24(0.30)	0.63
	3 ₂₁ – 2 ₂₀	3.51(0.37)	36.60(0.33)	5.94(0.75)	0.56
G14.20-0.19	3 ₀₃ – 2 ₀₂	7.99(0.34)	40.00(0.10)	4.66(0.23)	1.61
	3 ₂₂ – 2 ₂₁	1.63(0.23)	39.46(0.31)	4.71(0.87)	0.33
	3 ₂₁ – 2 ₂₀	1.61(0.20)	40.55(0.33)	4.63(0.52)	0.33
G14.33-0.64	3 ₀₃ – 2 ₀₂	19.66(0.23)	22.57(0.02)	3.86(0.06)	4.79
	3 ₂₂ – 2 ₂₁	5.89(0.21)	22.28(0.06)	3.82(0.17)	1.44
	3 ₂₁ – 2 ₂₀	4.50(0.19)	22.10(0.07)	3.45(0.17)	1.23
G15.66-0.50	3 ₀₃ – 2 ₀₂	5.86(0.24)	-5.14(0.10)	5.07(0.29)	1.09
	3 ₂₂ – 2 ₂₁
	3 ₂₁ – 2 ₂₀
G17.10+1.02	3 ₀₃ – 2 ₀₂	1.06(0.16)	19.94(0.22)	3.01(0.46)	0.33
	3 ₂₂ – 2 ₂₁
	3 ₂₁ – 2 ₂₀
G18.21-0.34	3 ₀₃ – 2 ₀₂	3.39(0.20)	46.09(0.18)	6.01(0.45)	0.53
	3 ₂₂ – 2 ₂₁
	3 ₂₁ – 2 ₂₀
G19.01-0.03	3 ₀₃ – 2 ₀₂	5.86(0.21)	59.67(0.09)	5.47(0.27)	1.00
	3 ₂₂ – 2 ₂₁
	3 ₂₁ – 2 ₂₀
G22.55-0.52	3 ₀₃ – 2 ₀₂	2.77(0.21)	75.66(0.17)	4.62(0.42)	0.56
	3 ₂₂ – 2 ₂₁
	3 ₂₁ – 2 ₂₀
G28.61-0.03	3 ₀₃ – 2 ₀₂	1.51(0.19)	47.92(0.35)	5.70(0.71)	0.26
	3 ₂₂ – 2 ₂₁
	3 ₂₁ – 2 ₂₀
G28.86+0.07	3 ₀₃ – 2 ₀₂	2.07(0.26)	98.43(0.16)	3.30(0.47)	0.59
		4.69(0.26)	103.30(0.11)	4.11(0.26)	1.07

Table 2. continued

Sources	Transition	$\int T_{\text{mb}} dv$ K km s ⁻¹	V_{lsr} km s ⁻¹	FWHM km s ⁻¹	T_{mb} K
G28.86+0.07	$3_{22} - 2_{21}$	0.96(0.17)	103.40(0.21)	2.49(0.55)	0.36
	$3_{21} - 2_{20}$	1.31(0.17)	103.30(0.18)	2.70(0.44)	0.46
G30.70-0.07	$3_{03} - 2_{02}$	9.21(0.23)	90.25(0.05)	4.67(0.15)	1.86
	$3_{22} - 2_{21}$	2.47(0.17)	89.92(0.14)	4.34(0.35)	0.53
	$3_{21} - 2_{20}$	1.86(0.19)	90.43(0.16)	3.37(0.38)	0.51
G31.40-0.26	$3_{03} - 2_{02}$	11.81(0.17)	86.70(0.03)	4.86(0.08)	2.29
	$3_{22} - 2_{21}$	1.74(0.16)	87.17(0.19)	3.85(0.36)	0.43
	$3_{21} - 2_{20}$	2.00(0.20)	87.00(0.19)	3.82(0.47)	0.49
G35.03+0.35	$3_{03} - 2_{02}$	9.53(0.21)	52.70(0.06)	5.16(0.12)	1.73
	$3_{22} - 2_{21}$	2.29(0.26)	52.55(0.38)	6.64(0.93)	0.33
	$3_{21} - 2_{20}$	2.23(0.21)	52.92(0.23)	4.76(0.47)	0.44
G35.19-0.74	$3_{03} - 2_{02}$	16.43(0.29)	36.42(0.05)	6.68(0.14)	2.31
	$3_{22} - 2_{21}$	2.31(0.21)	36.20(0.16)	4.01(0.54)	0.54
	$3_{21} - 2_{20}$	1.49(0.17)	36.12(0.18)	2.98(0.39)	0.47
G37.87-0.40	$3_{03} - 2_{02}$	10.76(0.94)	60.93(0.27)	6.48(0.68)	1.56
	$3_{22} - 2_{21}$
	$3_{21} - 2_{20}$

2. Selection of targets, observations, and data reduction

We have selected 30 massive clumps of the Galactic disk at various stages of high-mass star formation and with strong NH₃ emission from the ATLASGAL survey (see Table 1). At Effelsberg, the NH₃ (J, K) = (1,1), (2,2), and (3,3) lines have been measured by Wienen et al. (2012) who determined kinetic temperatures, based on the NH₃ (2,2)/(1,1) ratio, ranging from 11 to 61 K. The sample of high-mass star forming clouds at various evolutionary stages contains infrared dark clouds (IRDCs), clouds hosting extended green objects (EGOs) that are thought to trace outflows and are generally thought to be in an early stage of massive star formation (Cyganowski et al. 2008, 2011; Chen et al. 2013a,b), and clouds associated with HII regions based on the SIMBAD Astronomical Database¹.

Sources observed are listed in Table 1. Our observations were carried out in 2015 April, July, and October with the 15m James Clerk Maxwell Telescope telescope (JCMT) on Mauna Kea. The beam size is $\sim 23''$ and the main-beam efficiency is $\eta_{\text{mb}} = T_{\text{a}}^*/T_{\text{mb}} \simeq 0.7$ at 218 GHz². The para-H₂CO $J_{K_A K_C} = 3_{03}-2_{02}$, $3_{22}-2_{21}$, and $3_{21}-2_{20}$ transitions have rest frequencies of 218.222, 218.475, and 218.760 GHz, respectively, which are measured simultaneously by employing the ACSIS digital autocorrelation spectrometer with the special backend configuration RxA_H₂CO_250x3 allowing for three windows, each with a bandwidth of 250 MHz³. This provides a velocity resolution of 0.084 km s⁻¹ for para-H₂CO ($3_{03}-2_{02}$ and $3_{22}-2_{21}$) and 0.042 km s⁻¹ for para-H₂CO ($3_{21}-2_{20}$); CH₃OH ($4_{22}-3_{12}$) at 218.440 GHz is also observed together with para-H₂CO ($3_{22}-2_{21}$).

Data reduction for spectral lines was performed using Starlink⁴ and GILDAS⁵. To enhance signal-to-noise ratios (S/N) in individual channels, we smoothed contiguous channels to a velocity resolution ~ 0.33 km s⁻¹.

3. Results

Of the 30 massive clumps observed (see Table 1), 25 are detected in the para-H₂CO ($3_{03}-2_{02}$) line. Among the 25 para-H₂CO ($3_{03}-2_{02}$) detections, 10 also show the para-H₂CO ($3_{22}-2_{21}$) and ($3_{21}-2_{20}$) lines, while 18 also exhibit emission from the CH₃OH ($4_{22}-3_{12}$) line (218.440 GHz), which is well separated from the para-H₂CO ($3_{22}-2_{21}$) transition in all cases. The para-H₂CO and the CH₃OH line spectra are presented in Figures A.1 and A.2. Line parameters are listed in Tables 2 and 3, where integrated intensity ($\int T_{\text{mb}} dv$), local standard of rest velocity (V_{lsr}), line width (FWHM), and peak antenna brightness temperature (T_{mb}) were obtained from Gaussian fits. Five sources show no H₂CO and CH₃OH, namely G10.99-0.08, G13.28-0.3, G30.24+0.57, G31.70-0.49, and G34.37-0.66. G30.24+0.57 has a low H₂ column density of 2.2×10^{22} cm⁻² (Wienen et al. 2012). G10.99-0.08, G13.28-0.3, G31.70-0.49, and G34.37-0.66 are associated with infrared dark clouds, which have a low kinetic temperature in the range of 10.5 – 13.5 K. This suggests that para-H₂CO and CH₃OH are excited with difficulty in these low-density and/or low-temperature regions. Nevertheless, high detection rates of H₂CO ($\sim 83\%$) and CH₃OH ($\sim 60\%$) indicate that the two molecular species are commonly formed in the massive clumps of our sample.

3.1. H₂CO column density

To determine the para-H₂CO column densities and gas kinetic temperatures, we use the RADEX non-LTE model (van der Tak et al. 2007) offline code⁶ with collision rates from Wiesenfeld & Faure (2013). The RADEX code needs five input parameters: background temperature, kinetic temperature, H₂ density, para-H₂CO column density, and line width. For the background temperature, we adopt 2.73 K. Model grids for the para-H₂CO lines encompass 40 densities ($n(\text{H}_2) = 10^3 - 10^8$ cm⁻³), 40 para-H₂CO column densities ($N(\text{para-H}_2\text{CO}) = 10^{12} - 10^{16}$ cm⁻²), and 40 temperatures ranging from 10 to 110 K. For the line width, we use the observed line width value.

¹ <http://simbad.u-strasbg.fr/simbad/>

² <http://www.eaobservatory.org/jcmt/instrumentation/heterodyne/txa>

³ <http://www.eaobservatory.org/jcmt/instrumentation/heterodyne/acsis/>

⁴ <http://starlink.eao.hawaii.edu/starlink>

⁵ <http://www.iram.fr/IRAMFR/GILDAS>

⁶ <http://var.sron.nl/radex/radex.php>

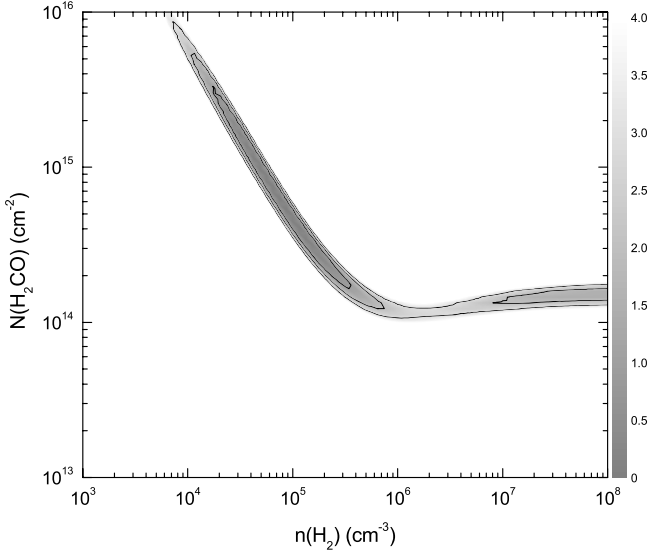


Fig. 1. Example of RADEX Non-LTE modeling of the $N(\text{H}_2\text{CO})$ – $n(\text{H}_2)$ relation for a kinetic temperature of 40 K. The source is G5.89-0.39. Contours enclose regions of low reduced χ^2_{red} based on $3_{03}-2_{02}$ and $3_{22}-2_{21}$ para- H_2CO brightness temperatures. Contours are $\chi^2_{\text{red}} = 3, 2$, and 1 .

Table 3. CH_3OH ($4_{22}-3_{12}$) spectral parameters.

Sources	$\int T_{\text{mb}} dv$ K km s ⁻¹	V_{lsr} km s ⁻¹	FWHM km s ⁻¹	T_{mb} K
G5.89-0.39	7.66(0.21)	9.52(0.06)	4.75(0.15)	1.51
G5.90-0.44	...	9.89(0.16)
G5.97-1.36	0.33(0.09)	22.63(0.12)	1.01(0.27)	0.31
G6.91-0.22	1.16(0.17)	21.00(0.27)	3.96(0.69)	0.27
G9.21-0.20	0.59(0.13)	42.11(0.16)	1.43(0.40)	0.39
G9.88-0.75	0.93(0.17)	28.18(0.29)	3.33(0.80)	0.26
G11.92-0.61	1.81(0.49)	35.78(0.31)	4.69(2.31)	0.36
G12.43-1.11	1.79(0.24)	39.52(0.23)	3.58(0.62)	0.47
G12.68-0.18	1.66(0.31)	54.49(0.52)	5.79(1.68)	0.27
G12.91-0.26	6.51(0.39)	37.70(0.16)	5.43(0.40)	1.13
G14.20-0.19	2.83(0.30)	39.94(0.25)	5.14(0.66)	0.51
G14.33-0.64	8.54(0.36)	22.01(0.07)	3.51(0.19)	2.29
G19.01-0.03	1.87(0.21)	59.93(0.24)	4.64(0.70)	0.39
G28.86+0.07	2.80(0.29)	103.10(0.19)	3.88(0.50)	0.67
G30.70-0.07	6.49(0.27)	90.06(0.10)	4.63(0.24)	1.31
G31.40-0.26	3.94(0.24)	87.12(0.14)	4.71(0.35)	0.79
G35.03+0.35	1.91(0.27)	52.99(0.36)	4.97(0.77)	0.36
G35.19-0.74	3.64(0.34)	35.96(0.22)	4.96(0.60)	0.69

We ran RADEX to obtain beam averaged para- H_2CO column densities and calculated the behavior of the χ^2_{red} value of the observed $3_{03}-2_{02}$ and $3_{22}-2_{21}$ (or $3_{21}-2_{20}$) para- H_2CO line brightness temperatures (see Figure 1). The value of χ^2_{red} is defined as

$$\chi^2_{\text{red}} = \sum_i \frac{(T_{\text{R(obs)}_i} - T_{\text{R(mod)}_i})^2}{\sigma_{T_{\text{R(obs)}_i}}^2}, \quad (1)$$

where $T_{\text{R(obs)}_i}$ and $T_{\text{R(mod)}_i}$ represent the observed main beam brightness temperatures (T_{mb}) and RADEX non-LTE modeled brightness temperatures, and $\sigma_{T_{\text{R(obs)}_i}}^2$ represents the uncertainty in $T_{\text{R(obs)}_i}$ including the rms noise in the spectra and the absolute temperature calibration uncertainty. One degree of freedom is used to the fit χ^2_{red} value. The reduced χ^2_{red} value depends of course on T_{kin} , but also to a lesser degree on H_2 density and para- H_2CO column density. To provide a feeling of the related uncer-

tainties, we take as an example source G5.89-0.39 (see Figure 1), which is a typical case. This figure shows that χ^2_{red} depends on the H_2 density and para- H_2CO column density at low densities ($n(\text{H}_2) < 10^6 \text{ cm}^{-3}$), while the kinetic temperature is kept constant at $\sim 40 \text{ K}$ (which is close to the actual temperature, see below). For higher densities, χ^2_{red} decreases only slowly with H_2 density. The entire plot provides a lower limit to the column density at $N(\text{H}_2\text{CO}) \sim 10^{14} \text{ cm}^{-2}$.

The H_2 density of the ATLASGAL clumps is $\sim 10^5 \text{ cm}^{-3}$ (Beuther et al. 2002; Motte et al. 2003; Wienen et al. 2012). As can be seen in Figure 1, our characteristic source G5.89-0.39 also shows the lowest χ^2_{red} values near this density, so we adopt an H_2 volume density of $n(\text{H}_2) = 10^5 \text{ cm}^{-3}$. The results are listed in Table 4. Including all sources, the $N(\text{para-}\text{H}_2\text{CO})$ range is $0.4 - 47 \times 10^{13} \text{ cm}^{-2}$ with an average of $6.5 \times 10^{13} \text{ cm}^{-2}$, which agrees with the results from other star forming regions and from protostellar cores (Mangum et al. 1993; Hurt et al. 1996; Watanabe & Mitchell 2008). At densities $n(\text{H}_2) = 10^5 \text{ cm}^{-3}$, the fractional abundance $N(\text{para-}\text{H}_2\text{CO})/N(\text{H}_2)$ becomes $0.4 - 5.4 \times 10^{-10}$, where $N(\text{H}_2)$ is derived from the $870 \mu\text{m}$ continuum emission (Wienen et al. 2012).

The column densities of para- NH_3 derived from the (1,1) and (2,2) lines (Wienen et al. 2012), those of para- H_2CO (derived at density 10^5 cm^{-3}), and the fractional abundances of $N(\text{para-}\text{H}_2\text{CO})/N(\text{H}_2)$, $N(\text{para-}\text{NH}_3)/N(\text{H}_2)$, and $N(\text{para-}\text{NH}_3)/N(\text{para-}\text{H}_2\text{CO})$ with corresponding H_2 column density and kinetic temperature $T_{\text{kin}}(\text{NH}_3)$ are shown in Figure 2. The para- NH_3 column densities range from 10^{15} to 10^{16} cm^{-2} and show no correlation with the H_2 column density and gas kinetic temperature in the massive clumps (see Figure 2 (a, b)). Variations in the fractional abundance of $N(\text{para-}\text{NH}_3)/N(\text{H}_2)$ amount to nearly two orders of magnitude ($2.6 \times 10^{-8} - 1.5 \times 10^{-6}$). The $N(\text{para-}\text{NH}_3)/N(\text{H}_2)$ ratio decreases with increasing H_2 column density and kinetic temperature (see Figure 2 (c, d)). The para- H_2CO column density increases proportionally with the H_2 column density and gas kinetic temperature (see Figure 2 (a, b)). The fractional abundance of $N(\text{para-}\text{H}_2\text{CO})/N(\text{H}_2)$ remains stable with increasing H_2 column density and kinetic temperature (see Figure 2 (c, d)). Nevertheless, the scatter amounts to $0.4 - 5.4$, i.e., by more than a factor of 10. The relative abundances $N(\text{para-}\text{NH}_3)/N(\text{para-}\text{H}_2\text{CO})$ range from 4.9×10^0 to 7.4×10^2 and decrease with H_2 column density and kinetic temperature (see Figure 2 (e, f)). The stable fractional para- H_2CO abundances as a function of $N(\text{H}_2)$ and T_{kin} (see Figure 2 (c, d) indicates that H_2CO is a more reliable tracer of the H_2 column density than NH_3 .

We also derive averaged column densities and fractional abundances of para- NH_3 and para- H_2CO in the subsamples consisting of HII regions, EGOs, and IRDCs. For NH_3 , the average column densities $N(\text{para-}\text{NH}_3)$ are $1.84 (\pm 1.00) \times 10^{15}$, $2.32 (\pm 0.45) \times 10^{15}$, and $3.55 (\pm 2.00) \times 10^{15} \text{ cm}^{-2}$, with the errors representing the standard deviations of the mean. The fractional abundances $N(\text{para-}\text{NH}_3)/N(\text{H}_2)$ are $0.74 (\pm 0.25) \times 10^{-7}$, $0.74 (\pm 0.37) \times 10^{-7}$, and $2.06 (\pm 0.67) \times 10^{-7}$ in HII regions, EGOs, and IRDCs, respectively. For H_2CO , the average column densities $N(\text{para-}\text{H}_2\text{CO})$ are $1.16 (\pm 1.35) \times 10^{14}$, $1.04 (\pm 0.93) \times 10^{14}$, and $2.81 (\pm 2.00) \times 10^{13} \text{ cm}^{-2}$. Fractional abundances $N(\text{para-}\text{H}_2\text{CO})/N(\text{H}_2)$ are $3.32 (\pm 1.36) \times 10^{-10}$, $2.53 (\pm 1.21) \times 10^{-10}$, and $1.23 (\pm 0.66) \times 10^{-10}$ in HIIs, EGOs, and IRDCs. Average variations of fractional abundances of $N(\text{para-}\text{H}_2\text{CO})/N(\text{H}_2)$ in different stages of star formation amount to nearly a factor of 3, which is similar to the amount of change seen in the fractional abundance $N(\text{para-}\text{NH}_3)/N(\text{H}_2)$. Therefore, we confirm that H_2CO can be widely used as a probe to trace the dense gas

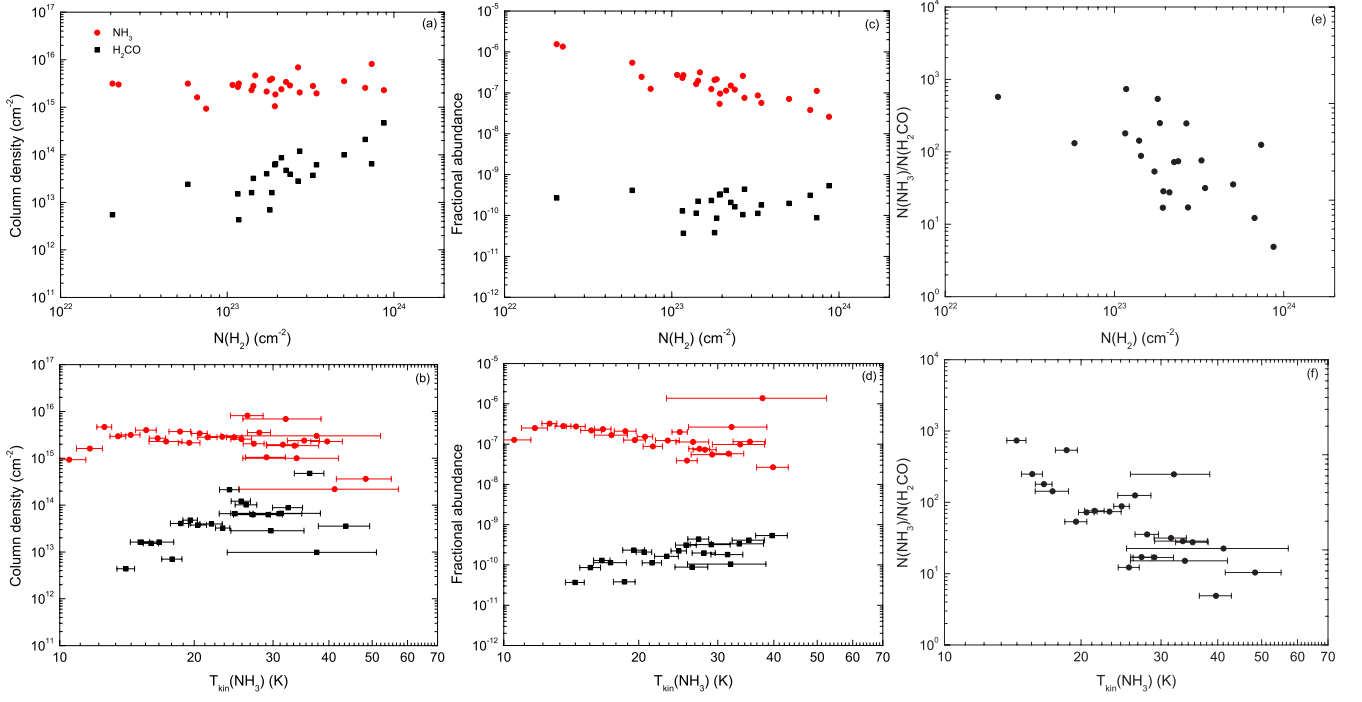


Fig. 2. Column densities of $N(\text{para-NH}_3)$ and $N(\text{para-H}_2\text{CO})$ (derived at density 10^5 cm^{-3}) (a, b), fractional abundance of $N(\text{para-NH}_3)/N(\text{H}_2)$ and $N(\text{para-H}_2\text{CO})/N(\text{H}_2)$ (c, d), and $N(\text{para-NH}_3)/N(\text{para-H}_2\text{CO})$ (e, f) vs. column density $N(\text{H}_2)$ and kinetic temperature $T_{\text{kin}}(\text{NH}_3)$.

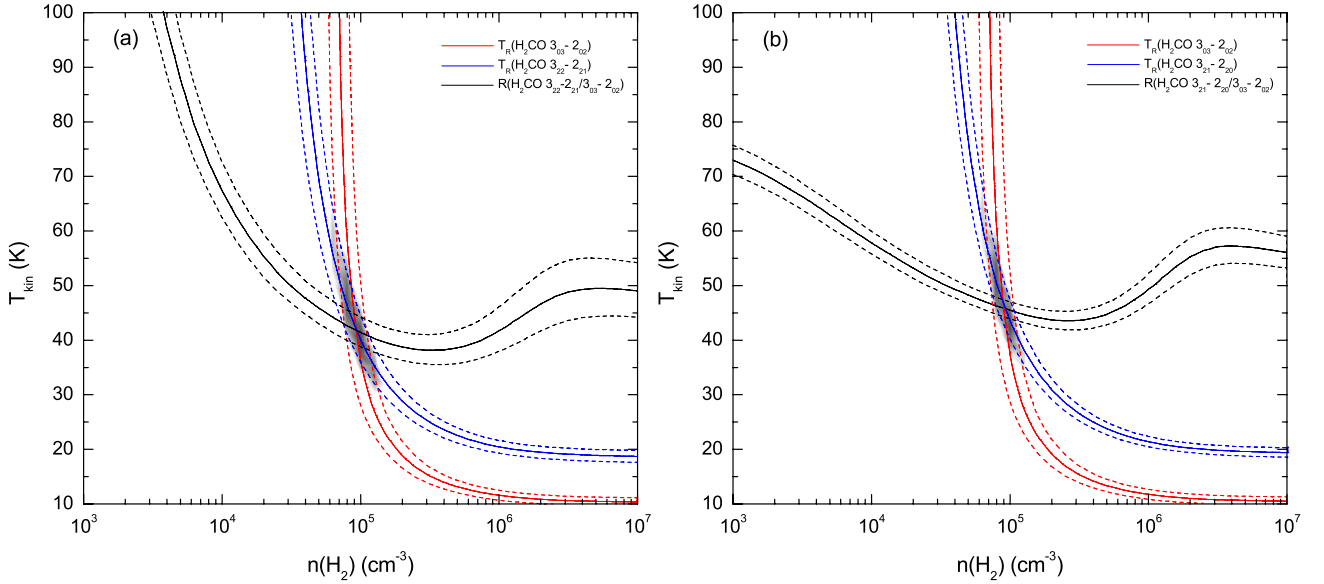


Fig. 3. Example of RADEX non-LTE modeling of the para- H_2CO kinetic temperature for G5.89-0.39. Para- H_2CO $3_{03}-2_{02}$ (red solid and dotted lines represent observed values and uncertainties), $3_{22}-2_{21}$ and $3_{21}-2_{20}$ (a and b, blue solid and dotted lines) line brightness temperatures and para- H_2CO $3_{22}-2_{21}/3_{03}-2_{02}$ and $3_{21}-2_{20}/3_{03}-2_{02}$ ratios (black solid and dotted lines). The gray region is characterized by $\chi^2_{\text{red}} < 1.5$ with density $n(\text{H}_2)$ and kinetic temperature T_{kin} for a para- H_2CO column density $4.7 \times 10^{14} \text{ cm}^{-2}$.

without drastic changes in abundance during various stages of star formation.

3.2. Kinetic temperature

The para- H_2CO ($3_{03}-2_{02}$) line is the strongest of the three 218 GHz para- H_2CO transitions. In order to avoid small uncertain values in the denominator, we used the para- H_2CO $3_{22}-2_{21}/3_{03}-2_{02}$ and $3_{21}-2_{20}/3_{03}-2_{02}$ ratios to derive the kinetic temperature.

The two ratios trace the kinetic temperature with an uncertainty of $\lesssim 25\%$ below 50 K (Mangum et al. 1993). An example is presented to show how the parameters are constrained by the reduced χ^2_{red} value, line brightness, and line ratio distribution of para- H_2CO in the $T_{\text{kin}}-n(\text{H}_2)$ parameter space in Figure 3. We used the column density derived at 10^5 cm^{-3} to constrain the kinetic temperature.

Our results are listed in Table 4. The para- H_2CO $3_{22}-2_{21}/3_{03}-2_{02}$ line ratio is sensitive to the gas density at spatial densities

Table 4. Para-H₂CO column densities and kinetic temperature.

Sources	$N(\text{para-H}_2\text{CO})$ $n(\text{H}_2)=10^5 \text{ cm}^{-3}$ cm^{-2}	Kinetic temperature		
		$3_{22-2_{21}}/3_{03-2_{02}}$ K	$3_{21-2_{20}}/3_{03-2_{02}}$ K	T_{LTE} K
G5.89-0.39	4.7×10^{14}	42^{+5}_{-5}	45^{+3}_{-2}	58
G5.90-0.44	6.2×10^{13}	28^{+6}_{-5}	36^{+4}_{-6}	24
G5.97-1.36	2.4×10^{13}
G6.91-0.22	1.6×10^{13}
G9.04-0.52	4.3×10^{12}
G9.21-0.20	6.9×10^{12}
G9.88-0.75	3.9×10^{13}
G11.92-0.61	3.7×10^{13}
G12.43-1.11	6.2×10^{13}
G12.68-0.18	2.8×10^{13}
G12.91-0.26	1.0×10^{14}	45^{+5}_{-3}	47^{+9}_{-7}	40
G14.20-0.19	4.7×10^{13}	53^{+9}_{-8}	61^{+14}_{-12}	58
G14.33-0.64	1.6×10^{14}	53^{+4}_{-4}	51^{+6}_{-4}	76
G15.66-0.50	3.2×10^{13}
G17.10+1.02	5.5×10^{12}
G18.21-0.34	1.6×10^{13}
G19.01-0.03	4.0×10^{13}
G22.55-0.52	1.5×10^{13}
G28.61-0.03	9.7×10^{12}
G28.86+0.07	3.5×10^{13}	41^{+8}_{-6}	51^{+12}_{-10}	47
G30.70-0.07	6.5×10^{13}	41^{+5}_{-5}	40^{+3}_{-2}	65
G31.40-0.26	8.7×10^{13}	41^{+3}_{-3}	49^{+5}_{-4}	36
G35.03+0.35	6.5×10^{13}	51^{+7}_{-6}	48^{+6}_{-6}	56
G35.19-0.74	1.2×10^{14}	37^{+4}_{-3}	30^{+6}_{-3}	34
G37.87-0.40	6.6×10^{13}

$n(\text{H}_2) < 10^5 \text{ cm}^{-3}$ (see Figure 3), so it seems that this line ratio is not quite as good as $3_{21-2_{20}}/3_{03-2_{02}}$ as a thermometer to trace kinetic temperature in the low-density regions of a molecular cloud. At high density $n(\text{H}_2) \gtrsim 10^5 \text{ cm}^{-3}$, the two ratios ($3_{22-2_{21}}/3_{03-2_{02}}$ and $3_{21-2_{20}}/3_{03-2_{02}}$) show a similar behavior to kinetic temperature and spatial density. The comparison of kinetic temperatures derived from both para-H₂CO $3_{22-2_{21}}/3_{03-2_{02}}$ and $3_{21-2_{20}}/3_{03-2_{02}}$ ratios suggests that the two ratios trace similar temperatures at a density of 10^5 cm^{-3} (see Table 4). The para-H₂CO $3_{22-2_{21}}$ and $3_{21-2_{20}}$ transitions, have similar energy above the ground state, $E_u \simeq 68 \text{ K}$, similar line brightness (see Table 2), and are often detected at the same time (e.g., Bergman et al. 2011; Wang et al. 2012; Lindberg & Jørgensen 2012; Ao et al. 2013; Immer et al. 2014; Treviño-Morales et al. 2014; Ginsburg et al. 2016); therefore, para-H₂CO $3_{22-2_{21}}/3_{03-2_{02}}$ and $3_{21-2_{20}}/3_{03-2_{02}}$ ratios are both good thermometers to determine kinetic temperature in dense regions ($n(\text{H}_2) \gtrsim 10^5 \text{ cm}^{-3}$). However, at lower densities, the $3_{21-2_{20}}/3_{03-2_{02}}$ ratio should be preferred.

The para-H₂CO line intensity ratios $3_{22-2_{21}}/3_{03-2_{02}}$ and $3_{21-2_{20}}/3_{03-2_{02}}$ can provide a measurement of the kinetic temperature of the gas in local thermodynamic equilibrium (LTE). The kinetic temperature can be calculated from para-H₂CO transitions assuming that the lines are optically thin, and originate from a high-density region (Mangum et al. 1993)

$$T_{\text{kin}} = \frac{47.1}{\ln(0.556 \frac{I(3_{03-2_{02}})}{I(3_{22-2_{21}})})}, \quad (2)$$

where $I(3_{03-2_{02}})/I(3_{22-2_{21}})$ is the para-H₂CO integrated intensity ratio. The results of the kinetic temperature calculations from the

para-H₂CO $3_{03-2_{02}}/3_{22-2_{21}}$ integrated intensity ratio are listed in Table 4. The kinetic temperatures derived from this method have an uncertainty of $\lesssim 30\%$ (Mangum et al. 1993). Considering this uncertainty, the temperatures derived from LTE and the RADEX non-LTE model are consistent (see Table 4).

4. Discussion

4.1. Comparison of H₂CO, CH₃OH, NH₃, and 870 μm emission

We compare the integrated intensities of para-H₂CO ($3_{03-2_{02}}$), CH₃OH ($4_{22-3_{12}}$), and NH₃ (1,1) with 870 μm emission in Figure 4. It shows that the molecules follow the 870 μm intensity distribution. The integrated intensities of para-H₂CO ($3_{03-2_{02}}$), CH₃OH ($4_{22-3_{12}}$), and NH₃ (1,1) are also compared in Figure 4. There is a good correlation between para-H₂CO ($3_{03-2_{02}}$) and CH₃OH integrated intensities (correlation coefficient $R^2 \sim 0.7$). Line widths of para-H₂CO ($3_{03-2_{02}}$) and CH₃OH also tend to be similar (see Tables 2 and 3). This suggests that the two molecules may trace similar regions and/or are chemically linked in their parent massive clumps.

H₂CO and CH₃OH are thought to be formed by successive hydrogenation of CO on grain surfaces: $\text{CO} \rightarrow \text{HCO} \rightarrow \text{H}_2\text{CO} \rightarrow \text{CH}_3\text{O} \rightarrow \text{CH}_3\text{OH}$ (Watanabe & Kouchi 2002; Woon 2002; Hidaka et al. 2004). Previous observations of para-H₂CO and CH₃OH in the Orion Bar photon-dominated region (PDR) have suggested that para-H₂CO traces the interclump material. CH₃OH is found mainly in the clumps, so that the two species trace different environments (Laurini et al. 2006, 2010). Our result differs from what is found for the Orion Bar, but is

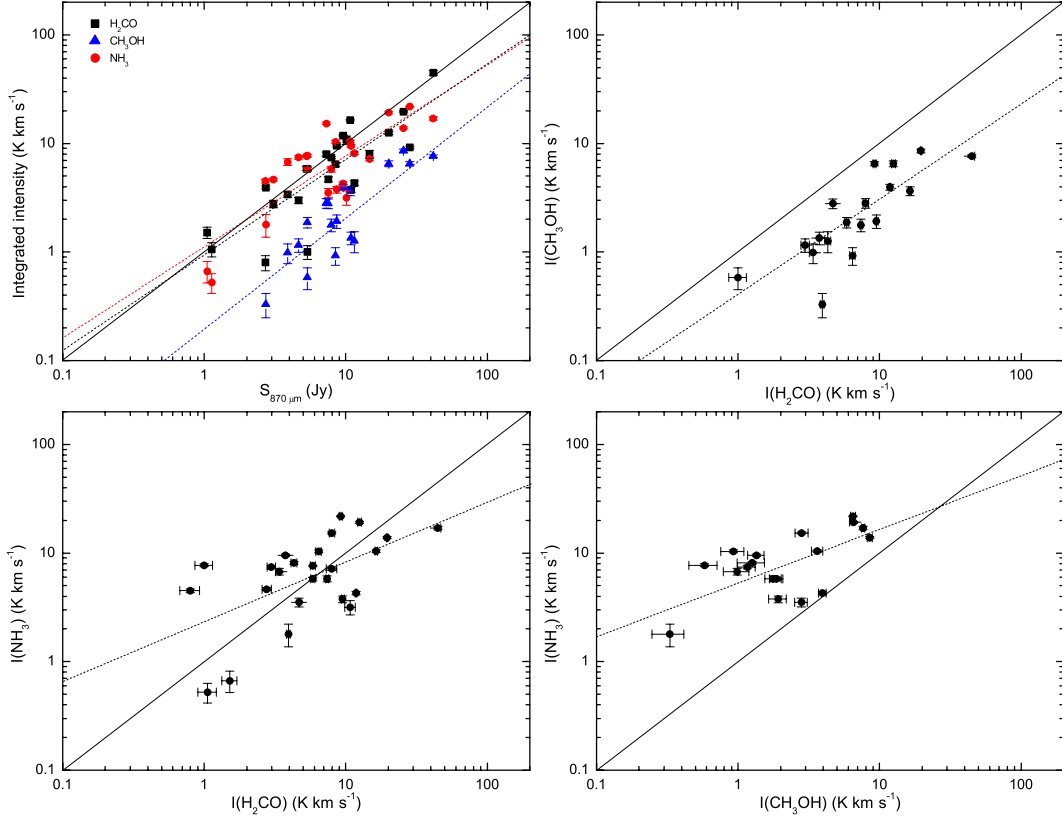


Fig. 4. Comparison of integrated intensities of para-H₂CO (3₀₃-2₀₂), CH₃OH (4₂₂-3₁₂), NH₃ (1,1), and 870 μm continuum flux densities. Dashed lines are the results from linear fits. Solid lines correspond to $Y = X$. Gauss fitted peak temperatures and line widths of NH₃ (1,1) are from Wienen et al. (2012). Assuming Gaussian profiles, we plot integrated intensities calculated with $\int T(v)dv = \sqrt{\pi/4\ln 2} \cdot T_{pk} \cdot \Delta V_{FWHM}$.

consistent with the majority of results where the two species are similarly distributed as in e.g., W3, CrA, L1157, W33, and NGC 2264 (Wang et al. 2012; Lindberg & Jørgensen 2012; Gómez-Ruiz et al. 2013; Immer et al. 2014; Cunningham et al. 2016). The likely reason is the different molecular environment. CH₃OH is more easily photodissociated than H₂CO in the PDRs.

For the integrated intensities of $I(\text{para-H}_2\text{CO})/I(\text{NH}_3)$ and $I(\text{CH}_3\text{OH})/I(\text{NH}_3)$, correlation coefficients (R^2) are 0.4 and 0.3, respectively, so they are only weakly correlated. Nearly all line widths of para-H₂CO (3₀₃-2₀₂) and CH₃OH are greater than those of NH₃ (1,1) (see Tables 2 and 3, and Tables 1 and 2 in Wienen et al. (2012)). The weak correlation can be explained if para-H₂CO and CH₃OH trace a higher density gas than NH₃ (1,1).

4.2. Comparison of kinetic temperatures derived from H₂CO and NH₃

For our massive clump samples with kinetic temperatures derived by para-H₂CO (3₂₁-2₂₀/3₀₃-2₀₂) and NH₃ (2,2)/(1,1), the kinetic temperature ranges for para-H₂CO from 30 to 61 K (average 46 ± 9 K), and for NH₃ from 21 to 48 K (average 32 ± 8 K), respectively. The comparison of kinetic temperature derived from the para-H₂CO (3₂₁-2₂₀/3₀₃-2₀₂) and the NH₃ (2,2)/(1,1) line ratios is shown in Figure 5. The kinetic temperatures derived from para-H₂CO and NH₃ agree in five sources, namely in G5.89-0.39, G5.90-0.44, G28.86+0.07, G31.40-0.26, and G35.19-0.74. Higher kinetic temperatures (difference > 10 K) traced by para-H₂CO as compared to NH₃ are found in G12.91-0.26, G14.20-0.19, G14.33-0.64, G30.70-0.07, and

G35.03+0.35. It seems that para-H₂CO traces a slightly higher temperature than NH₃ (2,2)/(1,1) in the massive clumps. The probable reason is that para-H₂CO may trace hotter and denser regions, while the NH₃ (2,2)/(1,1) line ratio traces cooler and more diffuse gas (Ginsburg et al. 2016). The different beam sizes for para-H₂CO (JCMT beam $\sim 23''$) and NH₃ (Effelsberg beam $\sim 40''$) data also have to be considered. The source sizes (FWHM) derived from para-H₂CO range from $20''$ to $31''$ (Csengeri et al. 2014), which match the JCMT beam but are smaller than the Effelsberg beam. The smaller JCMT beam size compared to Effelsberg might imply that the para-H₂CO data focus more on the inner active cloud cores than the NH₃ data do. Therefore, the determination of kinetic temperature differences may be influenced, to a certain degree, by beam size.

For an evaluation of whether beam size or other parameters play the dominant role in revealing differences between $T_{kin}(\text{para-H}_2\text{CO})$ and $T_{kin}(\text{NH}_3 (2,2)/(1,1))$, we have to check observational results in a systematic way. The NH₃ (1,1) and (2,2) transitions are sensitive to cold (10 – 40 K; Ho & Townes 1983; Mangum et al. 1992, 2013a) and dense ($\gtrsim 10^4 \text{ cm}^{-3}$; Rohlfs & Wilson 2004) gas. Previous para-H₂CO (3₂₂-2₂₁/3₀₃-2₀₂) and NH₃ (2,2)/(1,1) observations toward protostars, bipolar flows, submillimeter clumps, far infrared sources, active star formation sources, the Galactic center, Large Magellanic Clouds, and starburst galaxies show significantly different gas kinetic temperatures. Previous observed results with different telescopes are listed in Table 5. For L1527, L1551, N159W, and W3IRS4, the kinetic temperature difference still is < 30 K. Larger differences (> 45 K) are found in NGC2071 and NGC2024FIR5. The most significant difference is in the starburst galaxy M82

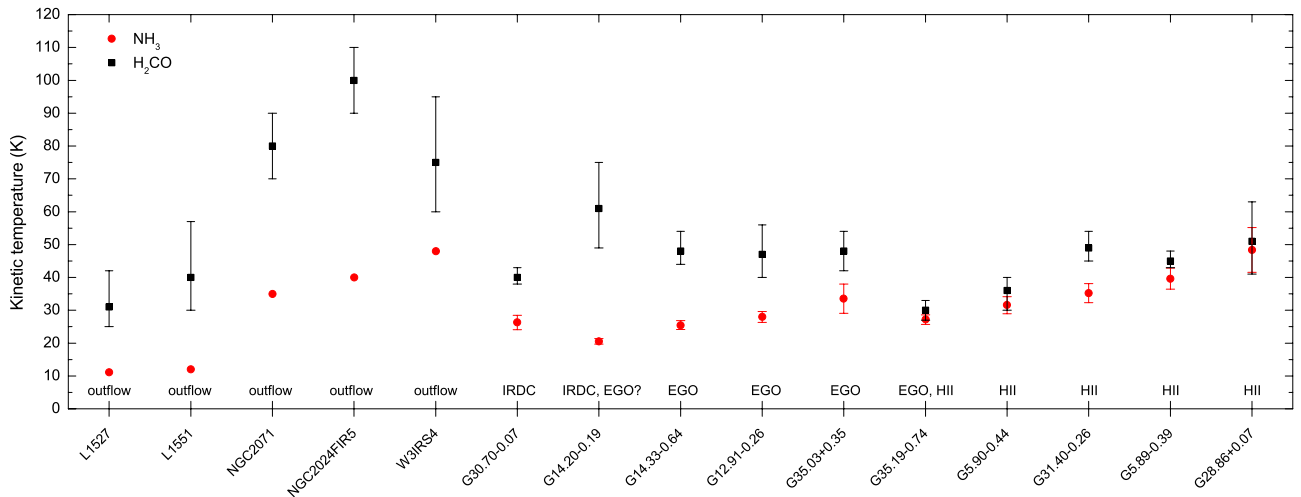


Fig. 5. Comparison of kinetic temperatures derived from para- H_2CO $3_{21-220}/3_{03-202}$ (black squares) and NH_3 (2,2)/(1,1) (red points) ratios. Para- H_2CO and NH_3 kinetic temperatures of L1551, L1527, NGC2071, NGC2024FIR5, and W3IRS4 are selected from Takano (1986), Mangum et al. (1993), Moriarty-Schieven et al. (1995), Jijina et al. (1999), and Watanabe & Mitchell (2008).

($T_{\text{kin}}(\text{NH}_3)$) deduced from (1,1)-(3,3), Weiß et al. 2001). Toward NGC2071 and M82, the NH_3 beam was the larger one, but in the case of NGC2024FIR5 we find the opposite. We also find the opposite in the case of N159W, $T_{\text{kin}}(\text{NH}_3) < T_{\text{kin}}(\text{para-}\text{H}_2\text{CO})$ in spite of a smaller ammonia beam. Therefore, the beam size difference between our JCMT para- H_2CO and the Effelsberg NH_3 data is likely not a dominant factor.

As shown in Figure 5, it seems that the differences between $T_{\text{kin}}(\text{para-}\text{H}_2\text{CO})$ and $T_{\text{kin}}(\text{NH}_3$ (2,2)/(1,1)) vary with evolutionary stage of the respective massive star formation region. The derived kinetic temperatures from para- H_2CO are distinctly higher than those from NH_3 (2,2)/(1,1) in the clumps associated with EGOs (difference > 14 K; G12.91-0.26, G14.20-0.19, G14.33-0.64, and G35.03+0.35). Similar temperature differences have been found in L1527, L1551, NGC2024FIR5, NGC2071, and W3IRS4, which are well-known outflow objects. The derived kinetic temperatures from NH_3 (2,2)/(1,1) may reflect an average temperature of cooler and more diffuse gas. The outflow/shock could heat the dense gas traced by H_2CO . Therefore, in these cases, para- H_2CO probes higher temperature gas which appears to be related to gas excited by star formation activities (e.g., outflows, shocks). The kinetic temperatures derived from para- H_2CO and NH_3 (2,2)/(1,1) are in agreement in the sources associated with HII regions (difference < 14 K; G5.89-0.39, G5.90-0.44, G28.86+0.07, and G31.40-0.26). This indicates that temperature gradients potentially probed by para- H_2CO and NH_3 (2,2)/(1,1) in different parts of the clouds are small. To conclude, para- H_2CO is a good thermometer, like NH_3 , to trace the gas kinetic temperature ($T_{\text{kin}}(\text{gas}) \gtrsim 30$ K) in the molecular environment surrounding HII regions. Large differences in kinetic temperatures between $T_{\text{kin}}(\text{para-}\text{H}_2\text{CO})$ and $T_{\text{kin}}(\text{NH}_3$ (2,2)/(1,1)) may indicate clouds in different evolutionary stages of massive star formation.

The kinetic temperatures based on para- H_2CO data disagree with the values obtained from NH_3 (1,1) and (2,2), but agree with the properties of the high-excitation component traced by CO in the starburst galaxy M82 (Mühle et al. 2007). Ao et al. (2013) found that the para- H_2CO kinetic temperatures are consistent with the temperatures derived from high- J NH_3 (Mauersberger et al. 1986) in the Galactic CMZ. Higher excited NH_3 lines commonly lead to higher kinetic temperatures. There-

Table 5. Previous results of observed para- H_2CO and NH_3 temperatures.

Sources	NH_3		para- H_2CO		Ref.
	Beam arcsec	T_{kin} K	Beam arcsec	T_{kin} K	
L1527	88	11	28	31^{+11}_{-6}	1,2
L1551	40	12	28	40^{+17}_{-10}	1,3
W3IRS4	40	48	30	75^{+20}_{-15}	3,4
NGC2071	88	35	23,30	80^{+15}_{-10}	3,4,5
NGC2024FIR5	3	40	23	100^{+10}_{-10}	3,6
N159W	9	16	23	29^{+5}_{-5}	7,8
M82	40	60	23	200	9,10

References. (1) Moriarty-Schieven et al. (1995); (2) Takano (1986); (3) Jijina et al. (1999); (4) Mangum et al. (1993); (5) Mitchell et al. (2001); (6) Watanabe & Mitchell (2008); (7) Heikkilä et al. (1999); (8) Ott et al. (2010); (9) Mühle et al. (2007); (10) Weiß et al. (2001).

fore, if higher NH_3 levels (e.g., NH_3 (2,2)/(4,4); Mangum et al. (2013a); Gong et al. (2015)) are also involved in measuring the kinetic temperatures, the values derived from para- H_2CO and NH_3 might become consistent in these sources where we have found a discrepancy. Thus detailed comparisons of T_{kin} values deduced from para- H_2CO and high- J NH_3 transitions would be meaningful.

4.3. Comparison of kinetic temperatures derived from the gas and the dust

The observed gas and dust temperatures do not agree in the Galactic CMZ (Güsten et al. 1981; Ao et al. 2013; Ott et al. 2014; Ginsburg et al. 2016; Immer et al. 2016). However, the temperatures derived from dust and gas are often in agreement in the active dense clumps of Galactic disk clouds (Dunham et al. 2010; Giannetti et al. 2013; Battersby et al. 2014). The dust temperatures are obtained from SED fitting to Herschel Hi-Gal data at 70, 160, 250, 350, and 500 μm and ATLASGAL data at 870 μm for our samples, following the method described in König et al. (submitted). The results are listed in

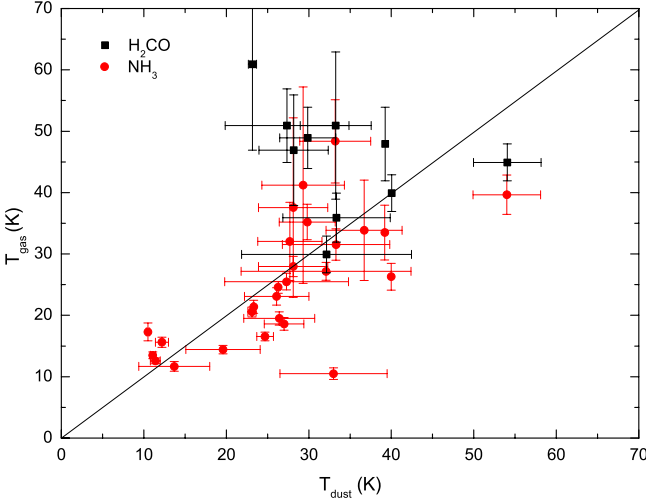


Fig. 6. Comparison of gas kinetic temperatures derived from para-H₂CO 3₂₁-2₂₀/3₀₃-2₀₂ (black squares) and NH₃ (2,2)/(1,1) (red points) ratios against the HiGal dust temperatures. The straight line indicates locations of equal temperatures. Two sources (G5.97-1.36 and G17.10+1.02) with particularly large $T_{\text{kin}}(\text{NH}_3)$ errors are not shown here.

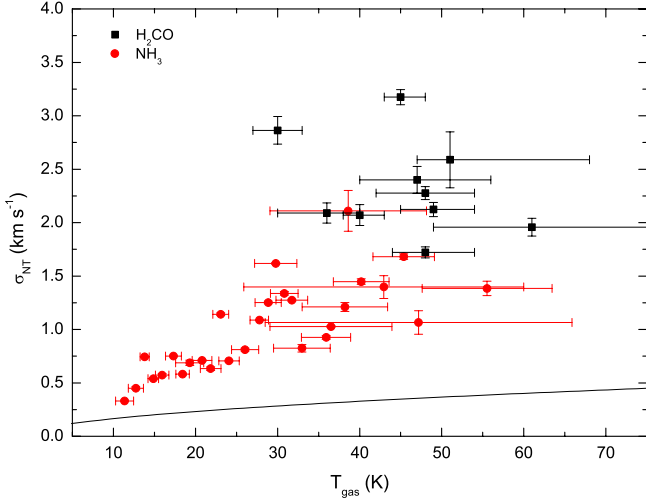


Fig. 7. Non-thermal velocity dispersion (σ_{NT}) vs. gas kinetic temperature for para-H₂CO (black squares) and NH₃ (red points). For the black squares, the gas kinetic temperatures were derived from para-H₂CO 3₂₁-2₂₀/3₀₃-2₀₂ line ratios. For the red points, they were obtained from the NH₃ (2,2)/(1,1) line ratios. The black line is the corresponding thermal sound speed. Two sources (G5.97-1.36 and G17.10+1.02) with particularly large $T_{\text{kin}}(\text{NH}_3)$ errors are not shown here.

Table 1. The derived kinetic temperature range is 11 – 54 K (average 26 ± 8 K). A comparison of gas kinetic temperature derived from para-H₂CO (3₂₁-2₂₀/3₀₃-2₀₂) and NH₃ (2,2)/(1,1) against HiGal dust temperatures is shown in Figure 6. For the temperatures derived from para-H₂CO, most sources (G12.91-0.26, G14.20-0.19, G14.33-0.64, G28.86+0.07, G31.40-0.26, and G35.03+0.35) show a higher temperature (difference > 9 K) than the HiGal dust temperature. The difference is due to the dust that may trace an average temperature covering a rather wide range of densities and is not as influenced by outflowing gas as para-H₂CO. The gas temperatures determined from NH₃ (2,2)/(1,1) agree with the HiGal dust temperatures considering

the uncertainties, which agrees with previous results found in the active dense clumps of Galactic disk clouds (Dunham et al. 2010; Giannetti et al. 2013; Battersby et al. 2014).

4.4. Non-thermal motion and turbulence

We computed thermal linewidth (σ_T), non-thermal velocity dispersion (σ_{NT}), thermal sound speed (a_s), and the ratio of thermal to non-thermal pressure (R_p) (Lada 2003). The σ_T , σ_{NT} , a_s , and R_p are given by

$$\sigma_T = \sqrt{\frac{kT_{\text{kin}}}{m_x}}, \quad (3)$$

$$\sigma_{NT} = \sqrt{\frac{\Delta V^2}{8 \ln 2} - \sigma_T^2}, \quad (4)$$

$$a_s = \sqrt{\frac{kT_{\text{kin}}}{\mu m_H}}, \quad (5)$$

$$R_p = \frac{a_s^2}{\sigma_{NT}^2}, \quad (6)$$

where k is the Boltzmann constant, T_{kin} is the kinetic temperature of the gas, m_x is the mass of the relevant molecule, ΔV is the measured FWHM linewidth of either the para-H₂CO 3₀₃-2₀₂ or the NH₃ (1,1) transitions, $\mu = 2.37$ is the mean molecular weight for molecular clouds, and m_H is the mass of the hydrogen atom. The derived values of σ_T , σ_{NT} , a_s , and R_p are listed in Table 6.

Comparisons of velocity dispersion, thermal sound speed, and kinetic temperature are shown in Figure 7 and Table 6. The derived non-thermal velocity dispersions of para-H₂CO and NH₃ are higher than the thermal linewidths. This indicates that the line broadening of para-H₂CO and NH₃ is dominated by non-thermal motions in these massive clumps. Para-H₂CO traces higher non-thermal motions (average $\sigma_{NT} = 2.1 \pm 0.6$ km s⁻¹) than those traced by NH₃ (for our selected sample, the average becomes $\sigma_{NT} = 1.1 \pm 0.4$ km s⁻¹; for all NH₃ samples observed by Wienen et al. (2012), the average becomes $\sigma_{NT} = 0.9 \pm 0.4$ km s⁻¹). Para-H₂CO linewidths appear to be affected strongly by non-thermal motions.

The average values of the Mach number (given as $M = \sigma_{NT}/a_s$) for para-H₂CO and NH₃ are 6.2 ± 1.5 and 3.4 ± 1.1 , which indicates that the velocity distributions within these massive clumps are significantly influenced by supersonic non-thermal components (e.g., turbulent motions, infall, outflow, rotation, shocks, and/or magnetic fields; Urquhart et al. 2015). The mean value of the Mach number derived from NH₃ agrees with the result (~ 3.2) of the Bolocam Galactic Plane Survey (BGPS) sources (Dunham et al. 2011). The determined ratio of thermal to non-thermal pressure, R_p (see Eq.(6)), ranges from 0.01 to 0.05 and the average becomes 0.03 ± 0.01 for para-H₂CO. For NH₃, we find values between 0.02 and 0.37 and the average becomes 0.11 ± 0.08 (all NH₃ samples observed by Wienen et al. (2012) yield 0.01–0.47 and the average becomes 0.10 ± 0.06). The low R_p values indicate that non-thermal pressure is dominant in these massive clumps.

It is expected that the correlation between kinetic temperature and line width is due to a conversion of turbulent energy into heat (Güsten et al. 1985; Molinari et al. 1996; Ginsburg et al. 2016; Immer et al. 2016). Recent para-H₂CO observations of the CMZ have shown that the warm dense gas is most likely heated by turbulence (Ao et al. 2013; Ginsburg et al. 2016; Immer et al.

Table 6. Thermal and non-thermal parameters.

Sources	NH ₃				H ₂ CO			
	σ_T km s ⁻¹	σ_{NT} km s ⁻¹	a_s km s ⁻¹	R_p	σ_T km s ⁻¹	σ_{NT} km s ⁻¹	a_s km s ⁻¹	R_p
G5.89-0.39	0.13	1.68	0.36	0.046	0.10	3.17	0.38	0.014
G5.90-0.44	0.12	0.92	0.32	0.121	0.08	2.09	0.34	0.027
G5.97-1.36	0.13	0.87	0.35	0.160	...	0.90
G6.91-0.22	0.08	0.75	0.22	0.090	...	2.20
G9.04-0.52	0.08	0.57	0.22	0.144	...	0.82
G9.21-0.20	0.09	0.70	0.24	0.121	...	1.18
G9.88-0.75	0.10	0.80	0.27	0.115	...	1.57
G10.99-0.08	0.08	0.74	0.20	0.074
G11.92-0.61	0.10	0.70	0.26	0.142	...	2.41
G12.43-1.11	0.11	0.82	0.31	0.141	...	1.44
G12.68-0.18	0.12	1.02	0.32	0.099	...	2.74
G12.91-0.26	0.11	1.27	0.30	0.056	0.11	2.40	0.39	0.026
G13.28-0.30	0.08	0.53	0.21	0.153
G14.20-0.19	0.10	1.14	0.26	0.051	0.12	1.96	0.44	0.051
G14.33-0.64	0.11	1.25	0.29	0.053	0.11	1.72	0.39	0.052
G15.66-0.50	0.11	1.08	0.28	0.068	...	2.03
G17.10+1.02	0.17	0.72	0.44	0.372	...	1.25
G18.21-0.34	0.09	0.68	0.24	0.120	...	2.13
G19.01-0.03	0.09	0.63	0.25	0.161	...	2.57
G22.55-0.52	0.09	0.58	0.23	0.161	...	1.82
G28.61-0.03	0.14	1.06	0.36	0.119	...	2.63
G28.86+0.07	0.15	1.38	0.39	0.082	0.10	2.59	0.41	0.025
G30.24+0.57	0.13	1.39	0.35	0.063
G30.70-0.07	0.11	1.61	0.29	0.033	0.10	2.07	0.36	0.030
G31.40-0.26	0.13	1.44	0.34	0.055	0.10	2.12	0.40	0.035
G31.70-0.49	0.07	0.44	0.19	0.191
G34.37-0.66	0.07	0.32	0.18	0.323
G35.03+0.35	0.12	1.20	0.33	0.075	0.11	2.27	0.39	0.030
G35.19-0.74	0.11	1.33	0.30	0.049	0.10	2.86	0.31	0.012
G37.87-0.40	0.12	2.11	0.33	0.025	...	2.67

Notes. Columns 2–5 and 6–9 are thermal linewidth, non-thermal velocity dispersion, thermal sound speed, and the ratio of thermal to nonthermal pressure obtained from NH₃ (1,1) and para-H₂CO (3₀₃-2₀₂) with kinetic temperatures derived from the NH₃ (2,2)/(1,1) and para-H₂CO (3₂₁-2₂₀/3₀₃-2₀₂) line intensity ratios, respectively. Para-H₂CO non-thermal velocity dispersions without kinetic temperatures are deduced from $\sigma_{NT} = \Delta V/2.355$ (Pan & Padoan 2009), where ΔV is the measured FWHM linewidth.

2016). Clumps formed in turbulent molecular clouds are significantly affected by the temperature of the cloud material (Bethell et al. 2004). We examine whether there is a relationship between turbulence and temperature in our massive clumps. We adopt the non-thermal velocity dispersion of NH₃ and para-H₂CO as proxy for the turbulence, and the kinetic temperatures of NH₃ (2,2)/(1,1) and para-H₂CO (3₂₁-2₂₀/3₀₃-2₀₂) as the gas kinetic temperature. Figure 7 shows that the non-thermal velocity dispersion of NH₃ and para-H₂CO are significantly positively correlated with the gas kinetic temperature. This implies that those massive clumps are turbulent and the gas may be heated by turbulent heating.

5. Summary

We have measured the kinetic temperature with para-H₂CO ($J_{K_A K_C} = 3_{03}-2₀₂, 3₂₂-2₂₁, and 3₂₁-2₂₀) and compare the kinetic temperature derived from this formaldehyde 218 GHz line triplet with those obtained from ammonia for 30 massive star forming clumps using the 15m JCMT. The main results are the following:$

1. The integrated intensity distributions of para-H₂CO, CH₃OH, and NH₃ agree well with the 870 μ m intensity dis-

tributions. The integrated intensities and linewidths of H₂CO and CH₃OH are also consistent in our clumps. They may trace similar regions and/or be chemically linked, while the correlation with NH₃ is less pronounced.

2. Using the RADEX non-LTE model, we derive gas kinetic temperatures by modeling the measured para-H₂CO 3₂₂-2₂₁/3₀₃-2₀₂ and 3₂₁-2₂₀/3₀₃-2₀₂ line ratios. We find that the two ratios are good thermometers to trace kinetic temperatures in dense regions ($n(\text{H}_2) \gtrsim 10^5 \text{ cm}^{-3}$) of the massive clumps, while for lower densities the 3₂₁-2₂₀/3₀₃-2₀₂ line ratio should be preferred.
3. The gas kinetic temperature of the massive clumps measured by NH₃ (2,2)/(1,1) line ratios (Wienen et al. 2012) ranges from 11 to 61 K (average 27 ± 12 K). The derived dust temperature range from Herschel HiGal data is 11 – 54 K with an average of 26 ± 8 K. The gas kinetic temperature derived from para-H₂CO (3₂₁-2₂₀/3₀₃-2₀₂) line ratios of the massive clumps ranges from 30 to 61 K with an average of 46 ± 9 K, which is higher than that measured by the NH₃ (2,2)/(1,1) transitions and the dust emission.
4. A comparison of kinetic temperatures derived from para-H₂CO, NH₃ (2,2)/(1,1), and the dust emission indicates that in many cases para-H₂CO traces a similar kinetic temper-

ature to the NH_3 (2,2)/(1,1) transitions and the dust associated with the HII regions. Distinctly higher temperatures are probed by para- H_2CO in the clumps associated with outflows/shocks.

5. Kinetic temperatures obtained by para- H_2CO trace turbulence to a higher degree than NH_3 (2,2)/(1,1) in the massive clumps. The non-thermal velocity dispersions of para- H_2CO and, to a lesser degree, NH_3 are positively correlated with the gas kinetic temperature. The massive clumps are significantly influenced by supersonic non-thermal motions.

Acknowledgements. We thank the staff of the JCMT telescope for their assistance in observations. The authors are grateful for the helpful comments of the referee. We thank Jens Kauffmann and Yan Gong for valuable comments. This work was funded by The National Natural Science Foundation of China under grant 11433008 and The Program of the Light in China's Western Region (LCRW) under grant Nos.XBBS201424 and The National Natural Science Foundation of China under grant 11373062, and partly supported by the National Basic Research Program of China (973 program, 2012CB821802). C.H acknowledges support by a visiting professorship for senior international scientists of the Chinese Academy of Sciences (2013T2J0057). This research has used NASA's Astrophysical Data System (ADS).

References

- Ao, Y., Henkel, C., Menten, K. M., et al. 2013, *A&A*, 550, 135
- Bally, J., Stark, A. A., Wilson, R. W., & Henkel, C. 1987, *ApJS*, 65, 13
- Battersby, C., Bally, J., Dunham, M., Ginsburg, A., et al. 2014, *ApJ*, 786, 116
- Benson, P. J., & Myers, P. C. 1983, *ApJ*, 270, 589
- Bergman, P., Parise, B., Liseau, R., & Larsson, B. 2011, *A&A*, 527, 39
- Bethell, T. J., Zweibel, E. G., Heitsch, F., & Mathis, J. S. 2004, *ApJ*, 610, 801
- Beuther, H., Schilke, P., Menten, K. M., et al. 2002, *ApJ*, 566, 945
- Bieging, J. H., Wilson, T. L., & Downes, D. 1982, *A&AS*, 49, 607
- Caselli, P., Hasegawa, T. I., & Herbst, E. 1993, *ApJ*, 408, 548
- Chen, X., Gan, C. G., Ellingsen S. P., et al. 2013a, *ApJS*, 206, 9
- Chen, X., Gan, C. G., Ellingsen S. P., et al. 2013b, *ApJS*, 206, 22
- Cohen, R. J., & Few, R. W. 1981, *MNRAS*, 194, 711
- Cohen, R. J., Matthews, N., Few, R. W., et al. 1983, *MNRAS*, 203, 1123
- Colbert, J. W., Malkan, M. A., Clegg, P. E., et al. 1999, *ApJ*, 511, 721
- Contreras, Y., Schuller, F., Urquhart, J. S., et al. 2013, *A&A*, 549, 45
- Csengeri, T., Urquhart, J. S., Schuller, F., et al. 2014, *A&A*, 565, 75.
- Cunningham, N., Lumsden, S. L., Cyganowski, C. J., Maud, L. T., & Purcell, C. 2016, *MNRAS*, 458, 1742
- Cyganowski, C. J., Brogan, C. L., Hunter, T. R., et al. 2011, *ApJ*, 743, 56
- Cyganowski, C. J., Whitney, B. A., Holden, E., et al. 2008, *AJ*, 136, 2391
- Danby, G., Flower, D. R., Valiron, P., Schilke, P., et al. 1988, *MNRAS*, 235, 229
- Downes, D., Wilson, T. L., Bieging, J., & Wink, J. 1980, *A&AS*, 40, 379
- Dunham, M. K., Rosolowsky, E., Evans, N. J. II., et al. 2010, *ApJ*, 717, 1157
- Dunham, M. K., Rosolowsky, E., Evans, N. J. II., et al. 2011, *ApJ*, 741, 110
- Giannetti, A., Brand, J., Sánchez-Monge, Á., et al. 2013, *A&A*, 556, 16
- Ginsburg, A., Bally, J., Battersby, J., Youngblood, A., et al. 2015, *A&A*, 573, 106
- Ginsburg, A., Henkel, C., Ao, Y., Riquelme, D., et al. 2016, *A&A*, 586, 50
- Gómez-Ruiz, A. I., Hirano, N., Leurini, S., & Liu, S.-Y. 2013, *A&A*, 558, 94
- Gong, Y., Henkel, C., Spezzano, S., et al. 2015, *A&A*, 574, 56
- Green, S. 1991, *ApJS*, 76, 979
- Güsten, R., Walmsley, C. M., & Pauls, T. 1981, *A&A*, 103, 197
- Güsten, R., Walmsley, C. M., Ungerechts, H., et al. 1985, *A&A*, 142, 381
- Heikkilä, A., Johansson, L. E. B., & Olofsson, H. 1999, *A&A*, 344, 817
- Hidaka, H., Watanabe, N., Shiraki, T., et al. 2004, *ApJ*, 614, 1124
- Ho P. T. P., & Townes, C. H., 1983, *ARA&A*, 21, 239
- Hurt, R., Barsony, M., & Wootten, A. 1996, *ApJ*, 456, 686
- Immer, K., Galván-Madrid, R., König, C., et al. 2014, *A&A*, 572, 63
- Immer, K., Kauffmann, J., Pillai, T., et al. 2016, *arXiv*, 1607.03535
- Jijina, J., Myers, P. C., & Adams, Fred C. 1999, *ApJS*, 125, 161
- Johnstone, D., Boonman A. M. S. & van Dishoeck E. F. 2003, *A&A*, 412, 157
- Lada, C. J., Bergin, E. A., Alves, J. F., & Huard, T. L. 2003, *ApJ*, 586, 286
- Leurini, S., Parise, B., Schilke, P., Pety, J., & Rolfs, R. 2010, *A&A*, 511, 82
- Leurini, S., Rolfs, R., Thorwirth, S., et al. 2006, *A&A*, 454, 47
- Lindberg, J. E., & Jørgensen, J. K. 2012, *A&A*, 548, 24
- Mangum, J. G., Darling, J., Henkel, C., et al. 2013a, *ApJ*, 779, 33
- Mangum, J. G., Darling, J., Henkel, C., & Menten, K. M. 2013b, *ApJ*, 766, 108
- Mangum, J. G., Darling, J., Menten, K. M., & Henkel, C. 2008, *ApJ*, 673, 832
- Mangum, J. G., & Wootten, A. 1993, *ApJS*, 89, 123
- Mangum, J. G., Wootten A., & Mundy L. G., 1992, *ApJ*, 388, 467
- Mangum, J. G., Wootten, A., & Plambeck, R. L. 1993, *ApJ*, 409, 282
- Mangum, J. G., Wootten, A., Wadiak, E. J., & Loren, R. B. 1990, *ApJ*, 348, 542
- Mauersberger, R., Henkel, C., & Wilson, T. L. 1987, *A&A*, 173, 352
- Mauersberger, R., Henkel, C., Wilson, T. L., et al. 1986, *A&A*, 162, 199
- Mitchell, G. F., Johnstone, D., Moriarty-Schieven, G., et al. 2001, *ApJ*, 556, 215
- Molinari, S., Brand, J., Cesaroni, R., & Palla, F. 1996, *A&A*, 308, 573
- Moriarty-Schieven, G. H., Wannier, P. G., Mangum, J. G., Tamura, M., & Olmsted, V. K. 1995, *ApJ*, 455, 190
- Motte, F., Schilke, P., & Lis, D. C. 2003, *ApJ*, 582, 277
- Mühle, S., Seaquist, E. R., & Henkel, C. 2007, *ApJ*, 671, 1579
- Nummelin, A., Bergman, P., Hjalmarson, Å., et al. 1998, *ApJS*, 117, 427
- Ott, J., Henkel, C., Staveley-Smith, L., & Weiß, A. 2010, *ApJ*, 710, 105
- Ott, J., Weiß, A., Staveley-Smith, L., Henkel, C., et al. 2014, *ApJ*, 785, 16
- Pan, L., & Padoan, P. 2009, *ApJ*, 692, 594
- Rohlfs K., & Wilson T. L., 2004, *Tools of Radio Astronomy*. Springer, Berlin
- Schuller, F., Menten, K. M., Contreras, Y., et al. 2009, *A&A*, 504, 415
- Schulz, A., Güsten, R., Zylka, R., & Serabyn, E. 1991, *A&A*, 246, 570
- Siringo, G., Kreysa, E., Kovács, A., et al. 2009, *A&A*, 497, 945
- van der Tak, F. F. S., Black, J. H., Schier, F. L., et al. 2007, *A&A*, 468, 627
- Takano, T. 1986, *ApJ*, 303, 349
- Tang, X. D., Esimbek, J., Zhou, J. J., et al. 2013, *A&A*, 551, 28
- Treviño-Morales, S. P., Pilleri, P., Fuente, A., et al. 2014, *A&A*, 569, 19
- Urquhart, J. S., Figura, C. C., Moore, T. J. T., et al. 2015, *MNRAS*, 452, 4029
- Urquhart, J. S., Moore, T. J. T., Csengeri, T., et al. 2014, *MNRAS*, 443, 1555
- Walmsley, C. M., & Ungerechts, H. 1983, *A&A*, 122, 164
- Wang, Y., Beuther, H., Zhang, Q., et al. 2012, *ApJ*, 754, 87
- Watanabe, N., & Kouchi, A. 2002, *ApJ*, 571, 173
- Watanabe, T., & Mitchell, G. 2008, *AJ*, 136, 1947
- Weiß, A., Neininger, N., Henkel, C., et al. 2001, *ApJ*, 554L, 143
- Wienen, M., Wyrowski, F., Menten, K. M., et al. 2015, *A&A*, 579, 91
- Wienen, M., Wyrowski, F., Schuller, F., et al. 2012, *A&A*, 544, 146
- Wiesenfeld, L., & Faure, A. 2013, *MNRAS*, 432, 2573
- Woon, D. 2002, *ApJ*, 569, 541
- Zylka, R., Güsten, R., Henkel, C., & Batrla, W. 1992, *A&AS*, 96, 525

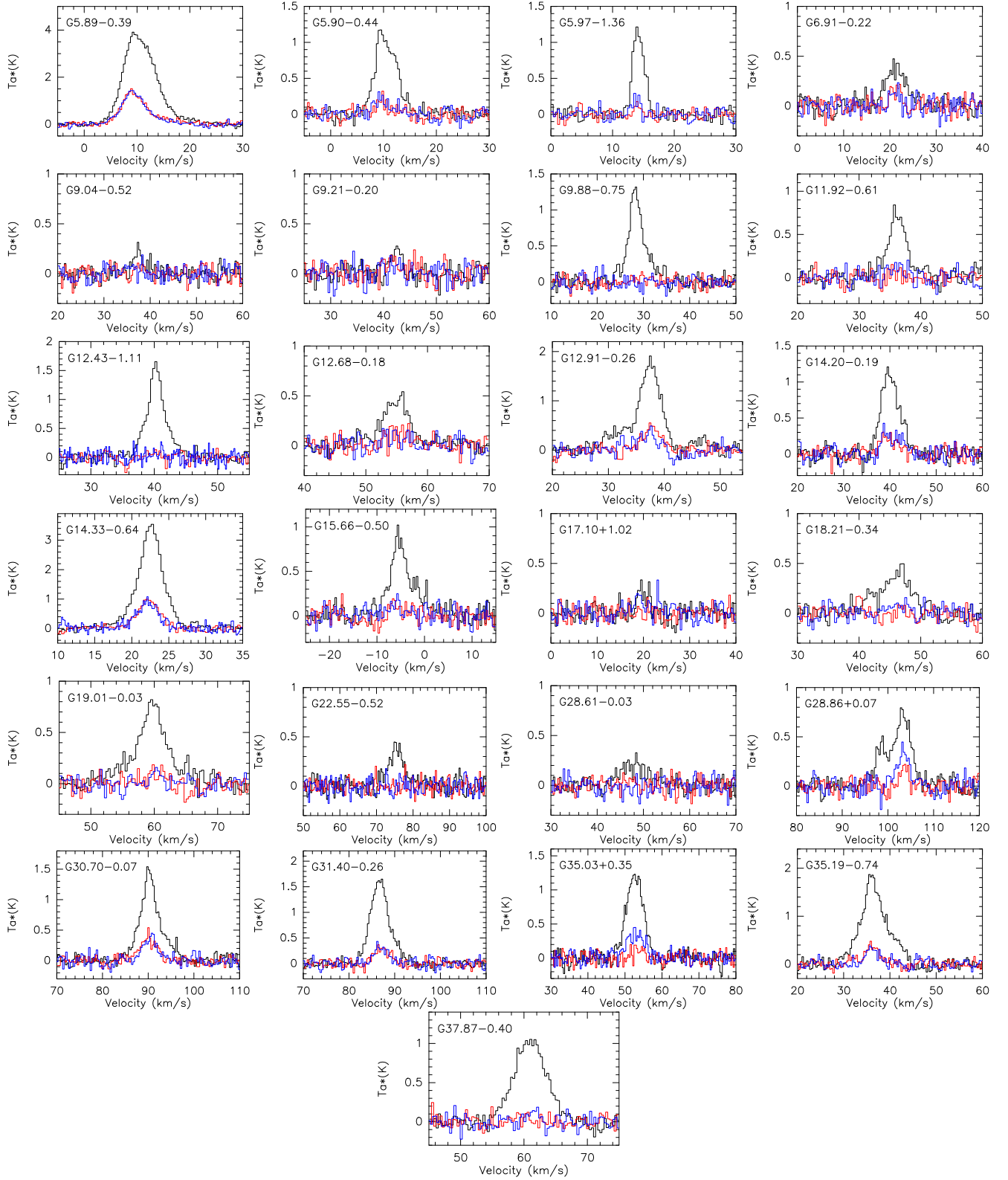
Appendix A: Spectra of para-H₂CO and CH₃OH.

Fig. A.1. Spectra of para-H₂CO. Black: para-H₂CO 3₀₃ – 2₀₂, Red: para-H₂CO 3₂₂ – 2₂₁, and Blue: para-H₂CO 3₂₁ – 2₂₀.

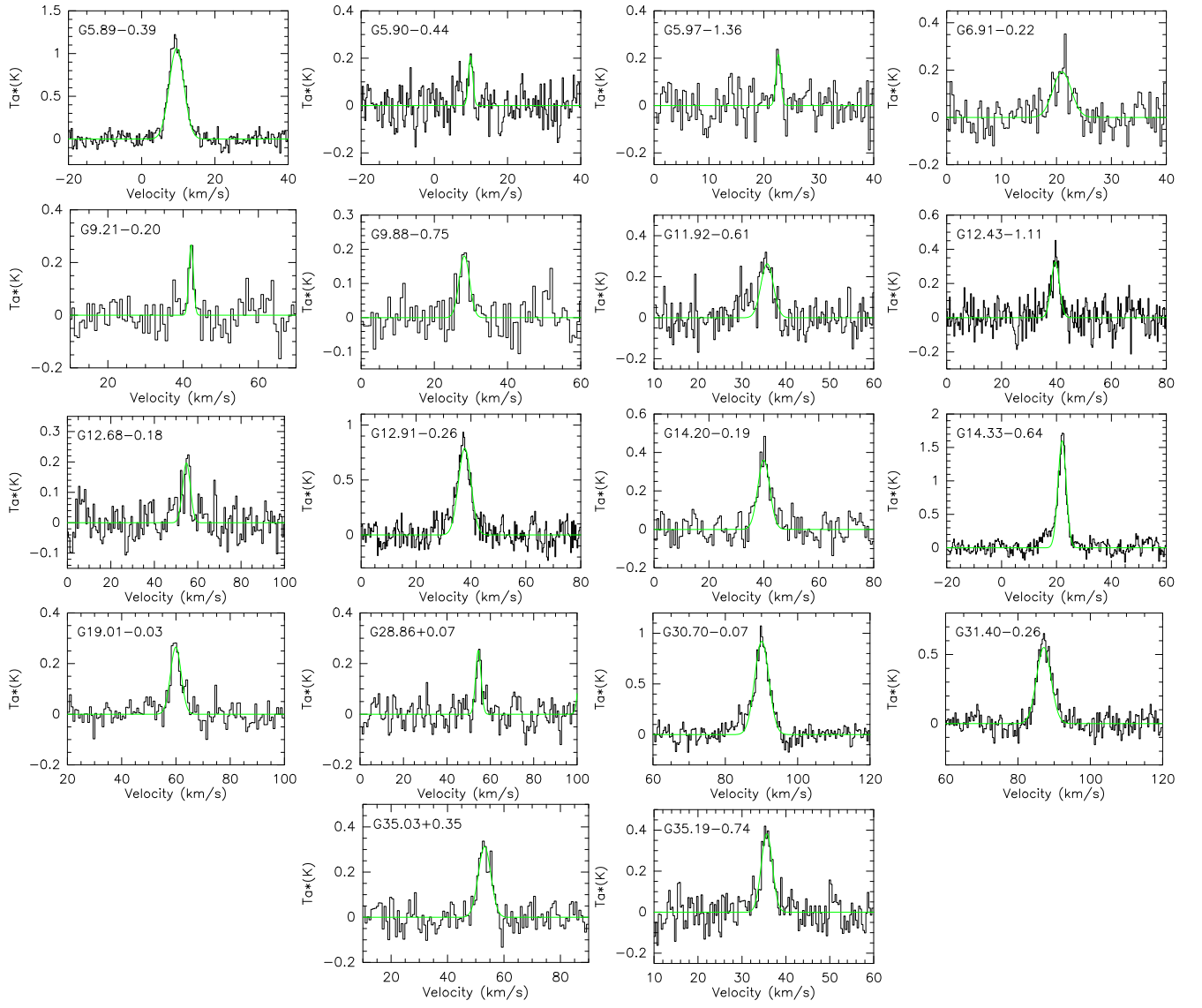


Fig. A.2. CH_3OH ($4_{22}-3_{12}$) spectra.